

# ISI Modeling and BER Performance for Rotating Light-Trail Image Sensor Communication

Shin Asaoka, Shan Lu, *Member, IEEE*, Zhengqiang Tang, and Takaya Yamazato, *Senior Member, IEEE*

**Abstract**—Image sensor communication (ISC) employing a propeller-LED transmitter encodes data along rotating light trails. We present an analytical framework that (i) constructs a single-LED, single-blink light trail model that maps optical power to pixel values, and (ii) integrates a probabilistic noise model to derive a closed-form bit-error rate (BER) using the  $Q$ -function. Trimodal pixel-value histograms motivate an adjacent-only inter-symbol interference (ISI) model in which the decision at segment  $j$  depends on adjacent segments. Applying a hardest-pair midpoint threshold yields per-segment BER and a general BER after marginalization. We further provide practical sufficiency conditions under which adjacent-only ISI is adequate, and validate its tightness against Monte Carlo simulations and experimental results. Using the analytical BER, we select the control angle that maximizes throughput while satisfying a target BER reliability constraint.

**Index Terms**—Image Sensor Communication (ISC), Optical Camera Communication (OCC), Rotating light trails, Adjacent-only ISI,  $Q$ -function, Threshold design, Propeller-LED

## I. INTRODUCTION

Image sensor communication (ISC) is a visible light communication (VLC) technique that uses an image sensor (camera) as the receiver [1], [2]. In ISC, the camera records the on-off states of light-emitting diodes (LEDs) as two-dimensional (2-D) image frames [3]. Owing to its spatial parallelism and selectivity, which enable interference rejection via simple image processing [4], [5], together with low cost and spatial privacy, ISC is attractive for short-range IoT links and screen-to-camera applications. Unmanned aerial vehicles (UAVs, drones) are increasingly deployed for disaster response and military missions, where radio-frequency links may be congested, regulated, or vulnerable to interception; as a result, VLC on drones has attracted growing interest [6], [7].

However, with static LEDs and frame-synchronous blinking, each on-off cycle is captured at most once per frame. Consequently, the per-LED symbol rate is fundamentally limited by the camera frame rate, and the per-frame throughput is further constrained by the number of LEDs within the field of view.

Leveraging a quadrotor's spinning propellers, a propeller-LED transmitter (P-Tx) mounts LEDs on a blade and modulates based on the rotation angle to increase the rate of ISC [8]. During exposure, the rotating emission integrates into an arcuate "light trail" that acts as a virtual extended source, enabling angle-mapped modulation without additional optics

Received 23 April 2025; accepted 4 May 2025. The associate editor is Dr. Sotiris Tegos. This work was supported by JSPS KAKENHI Grant Number 25K00371 and Telecommunications Advancement Foundation, Japan. (Corresponding author: Shan Lu.)

S. Asaoka, S. Lu and T. Yamazato are with Department of Information and Communication Engineering, Graduate School of Engineering, Nagoya University, Nagoya, 464-8601, Japan. (Email: shan.lu.jp@ieec.org.)

Zhengqiang Tang are with Dept of Elec. and Elec. Eng., Shizuoka University, Shizuoka Japan.

or tight synchronization and thereby increasing throughput. By partitioning the  $2\pi$  angular range into  $J$  sectors and mapping symbols to these angular segments, the P-Tx embeds  $J$  parallel pieces of information within a single image frame, achieving high-capacity transmission with only a small number of LEDs [9]. The key advantage is breaking the frame-rate bottleneck, enabling high-density communication. Thus, we position this as a low-rate, high-robustness method for scenarios like disaster monitoring and RF-restricted environments. While P-Tx VLC systems have been validated experimentally, theoretical analysis is scarce. Key parameters like rotation angle  $\Delta\theta = 2\pi/J$  have been chosen empirically to balance throughput and reliability [8], leaving BER behavior and design suboptimal.

In this paper, we provide an end-to-end analysis and design framework for P-Tx-based ISC. The main contributions are:

(1) **Single-LED single-blink model:** We develop a single-LED single-blinking light trail model that maps instantaneous optical transmit power of a single LED to the pixel values through the LOS channel, defocus blur, and the camera.

(2) **Adjacent-only ISI modeling and closed-form BER:** Guided by the observed multi-peak pixel-value histograms, we formulate an adjacent-only ISI model for light trail segments. With a *hardest-pair midpoint* decision threshold, we derive a closed-form BER expression in terms of the  $Q$ -function and validate its tightness against Monte Carlo simulations and experiments.

(3) **Design of the control angle  $\Delta\theta$ :** Using the analytic BER, we optimize  $\Delta\theta$  under a target-BER (reliability) constraint and demonstrate throughput maximization consistent with optimized  $\Delta\theta$ .

## II. SYSTEM MODEL: P-TX-BASED ISC

This section presents the P-Tx-based ISC system with light trails, which consists of a P-Tx, an optical channel, and a receiver (camera).

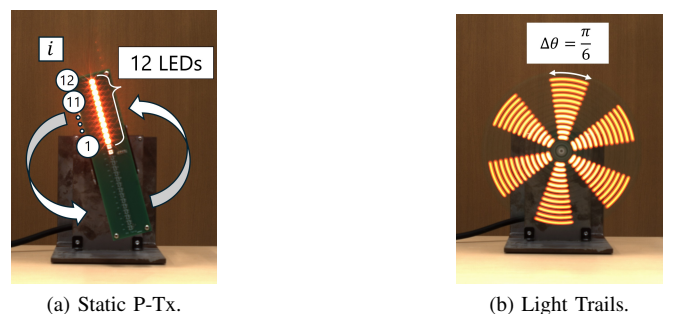


Fig. 1. Propeller LED Transmitter (P-Tx).

### A. P-Tx transmitter

We use a P-Tx, shown in Fig. 1. Twelve LEDs are arranged in a linear array with a spacing of 7-mm. For the  $i$ -th LED

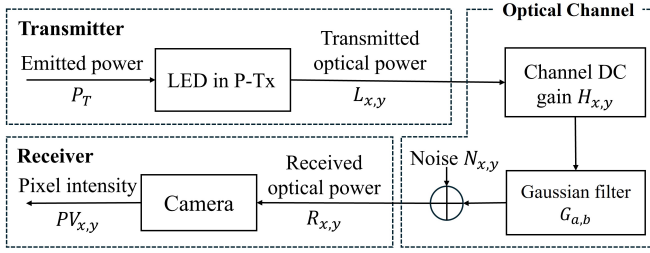


Fig. 2. Light trail source–channel–camera pipeline used in the analytical model.

( $i = 1, 2, \dots, 12$ ) at radius  $r_i$  from the rotation axis, the blinking state is controlled at each rotation angle  $\Delta\theta_i$  and the information is transmitted using On-Off Keying (OOK). Each full rotation has  $J_i = 2\pi/\Delta\theta_i$  bits. The data transmitted for the  $i$ -th LED at the angular position  $j \in \{0, \dots, J_i - 1\}$  is  $b_j^i$ .

We assume a parallel line-of-sight configuration in which the optical axes of the P-Tx and the camera are aligned. When the P-Tx rotation period is synchronized with the camera exposure time, the sensor integrates a full rotation into a single frame, producing a complete light trail [10].

### B. Demodulation of the receiver

For any LED  $i$ , the emitted light forms an approximately circular trace in the image plane. We partition this trace into  $J_i$  angular segments and, for each segment, extract a representative pixel value.

Let the image resolution be  $X \times Y$  with pixel coordinates  $(x, y)$ . Denote the centroid of the  $j$ -th segment for the LED  $i$  by  $(x_j^i, y_j^i)$ . We define the segment sample  $PV_{x_j, y_j}^i$  of the  $j$ -th segment by the pixel intensity at  $(x_j^i, y_j^i)$ .

The detected bit is obtained by threshold  $PV_{th}^i$  as

$$\hat{b}_j^i = \begin{cases} 1 & \text{if } PV_{x_j, y_j}^i > PV_{th}^i \\ 0 & \text{if } PV_{x_j, y_j}^i \leq PV_{th}^i \end{cases} \quad (1)$$

## III. SINGLE-LED SINGLE-BLINK LIGHT TRAIL MODEL

Since the pixel value is the fundamental observable for ISC demodulation, this section presents a **single-LED single-blink light trail model** that maps the instantaneous optical transmit power of one LED to pixel values through the LOS channel, defocus blur, and the camera, as illustrated in Fig. 2. Since we consider a single LED with single-blink, we **omit the index  $i$  and  $j$**  in this section.

1) *Transmitter*: Let  $P_{tot}$  be the total emitted power under constant illumination (i.e., when all  $J$  segments transmit “1”). If  $\bar{J}$  out of  $J$  segments are active, the emitted (transmitter-side) frame-level power is  $P_T = \bar{J} \cdot P_{tot}/J$ .

Let  $\mathbf{P} \in \mathbb{R}^{X \times Y}$  denote the (unnormalized) radiometric power distribution of the light trail on the sensor, with entries  $P_{x,y}$  obtained from the luminous-energy accumulation  $Q_{x,y}^{blink}$  along the blinking trail [11]:

$$P_{x,y} = \frac{Q_{x,y}^{blink}}{KV(\lambda)}. \quad (2)$$

where  $K$  is the maximum luminous efficacy coefficient and  $V(\lambda)$  is the relative luminous efficiency.

Let  $L_{x,y}$  denote the per-pixel incident optical energy at pixel  $(x, y)$  during the exposure. We allocate  $P_T$  across pixels proportionally to  $\mathbf{P}$  with

$$L_{x,y} = P_T \frac{P_{x,y}}{\sum_{u,v} P_{u,v}} \quad (3)$$

which guarantees  $\sum_{x,y} L_{x,y} = P_T$ .

2) *Optical channel and defocus blur*: We adopt a distance-dependent LOS channel [12]. The DC gain at pixel  $(x, y)$  is

$$H_{x,y} = \frac{A_p}{D_{x,y}^\gamma} R(\psi_{x,y}), \quad (4)$$

where  $D_{x,y}$  is the source–pixel distance,  $\gamma$  the path-loss exponent, and  $R(\psi)$  is the Lambertian radiant pattern with order  $m'$  as  $R(\psi) = \frac{m'+1}{2\pi} \cos^{m'}\psi$ .

The effective collection area is

$$A_p = \begin{cases} AT_s g \cos \epsilon_{x,y}, & 0 \leq \epsilon_{x,y} \leq \epsilon_\ell, \\ 0, & \epsilon_{x,y} > \epsilon_\ell, \end{cases} \quad (5)$$

with entrance pupil area  $A$ , filter transmittance  $T_s$ , lens gain  $g$ , angle of incidence  $\epsilon_{x,y}$ , and lens FoV  $\epsilon_\ell$ .

Defocus acts as a spatial low-pass filter that grows with distance [13]. We model it by a normalized discrete Gaussian kernel  $\{G_{a,b}\}$  of size  $q \times q$  and variance  $\sigma_g^2$ :

$$G_{a,b} = \frac{\exp(-(a^2 + b^2)/(2\sigma_g^2))}{\sum_{u=-(q-1)/2}^{(q-1)/2} \sum_{v=-(q-1)/2}^{(q-1)/2} \exp(-(u^2 + v^2)/(2\sigma_g^2))}. \quad (6)$$

The received optical power after blur is the 2-D convolution of per-pixel incident optical energy  $L_{x,y}$  with  $G$  scaled by  $H$ :

$$R_{x,y} = H_{x,y} \sum_{a,b} G_{a,b} L_{x-a, y-b}. \quad (7)$$

3) *Camera receiver*: The photon count at pixel  $(x, y)$  is

$$I_{x,y} = \frac{R_{x,y} + N_{x,y}}{Q_p}, \quad (8)$$

where  $R_{x,y}$  is the expected radiant energy accumulated during exposure and  $Q_p$  is the photon energy. Here  $N_{x,y}$  denotes the energy-domain fluctuation due to photon shot and readout noise. Under the normal approximation to the Poisson term,  $N_{x,y}$  is modeled as  $N_{x,y} \sim \mathcal{N}(0, \sigma_n^2)$ .

The camera pipeline (photoelectric conversion, amplification, A/D, gamma) is summarized by  $\Phi(\cdot)$ , and the pixel value at  $(x, y)$  is

$$PV_{x,y} = \Phi(I_{x,y}) = t\left(\frac{A_a A_c (V_{a,ref} - A_f (V_{ref} - Q_e A_n I_{x,y}))}{\text{raw}_{\max}}\right)^{1/g_a}, \quad (9)$$

where  $t(\cdot)$  denotes clipping to  $[0, 1]$  and the parameters are listed in Table I.

## IV. ISI MODELING AND ANALYTIC BER EVALUATION

### A. Motivation for ISI Model

Having introduced the single-blink light trail model, we now consider a single LED with multiple blinks. Fig. 3 shows the pixel intensity histogram for  $\Delta\theta = \pi/9$  and a 52 m link. The light trail is produced by a single LED that blinks

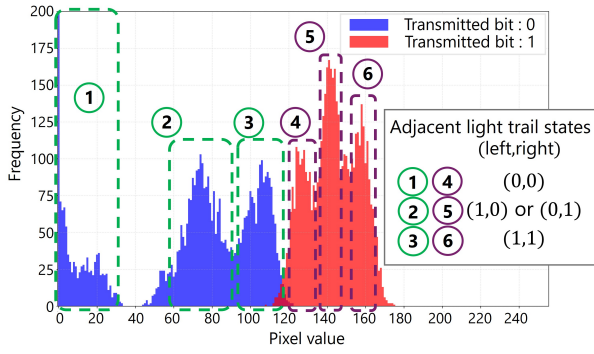


Fig. 3. Histogram of received pixel values in the simulation.

on/off randomly using OOK (5,000 random bits). For both symbol classes (0 and 1), the histogram is trimodal, with three peaks aligned with the adjacent-segment states (00), (01/10), and (11). The spread of each distribution in the histogram is caused by the blurring effect in Eq. (6), the noise shown in Eq. (8), and pixel value fluctuations associated with geometric positional errors of each light trail segment that arise when mapping continuous light trails onto a discrete 2D pixel distribution. This empirical pattern is consistent with inter-symbol interference (ISI) from the two adjacent light trail segments and motivates the ISI model developed below.

### B. Theoretical BER Performance Analysis

1) *BER analysis for interference model*: We consider an interference model in which the received power at  $(x_j, y_j)$  is modeled as a superposition of the  $j$ -th segment and its first neighbors, while the tail energy beyond the first neighbors is negligible:

$$R_{x_j, y_j} = b_{j-1} R_{x_j, y_j}^{j-1} + b_j R_{x_j, y_j}^j + b_{j+1} R_{x_j, y_j}^{j+1}. \quad (10)$$

where  $b_j \in \{0, 1\}$  is the on/off state of the  $j$ -th segment and the component powers  $R_{x_j, y_j}^{j \pm 1}$  are obtained from the physical model in Eq. (7) by activating only segment  $j \pm 1$  at  $(x_j, y_j)$ . Hence, Eq. (10) already reflects the effect of the isotropic Gaussian blur and the position-dependent geometric variation induced by pixel-grid alignment.

Following Eq. (8) in Sec. III-3, the camera maps the noisy received power to a pixel value via the response function  $\Phi(\cdot)$ . Since  $\Phi(\cdot)$  is nonlinear, additive power-domain noise becomes signal dependent in the pixel domain. For small noise (i.e., around a local operating point), we linearize  $\Phi(\cdot)$  at  $\mu_j \triangleq R_{x_j, y_j}^{\text{ISI}}/Q_p$  using a first-order Taylor expansion as:

$$\begin{aligned} PV_j^{\text{re}} &= \Phi\left(\frac{R_{x_j, y_j} + N_{x_j, y_j}}{Q_p}\right) \\ &\approx \Phi\left(\frac{R_{x_j, y_j}}{Q_p}\right) + \Phi'\left(\frac{R_{x_j, y_j}}{Q_p}\right) \frac{N_{x_j, y_j}}{Q_p}. \end{aligned}$$

When  $(b_{j-1}, b_j, b_{j+1})$  is fixed,  $\Phi(R_{x_j, y_j})$  is also fixed. Therefore, we define averaged value of  $PV_j^{\text{re}}$  and the equivalent pixel-domain noise as

$$\begin{aligned} PV_j^{\text{tot}}(b_{j-1}, b_j, b_{j+1}) &\triangleq \Phi(R_{x_j, y_j}) \\ N'_{x_j, y_j}(b_{j-1}, b_j, b_{j+1}) &\triangleq \Phi'\left(\frac{R_{x_j, y_j}}{Q_p}\right) \frac{N_{x_j, y_j}}{Q_p}. \end{aligned}$$

Since  $N_{x_j, y_j} \sim \mathcal{N}(0, \sigma_n^2)$ , the term above is zero-mean Gaussian with variance

$$\sigma_n'^2(b_{j-1}, b_j, b_{j+1}) = \left(\frac{\Phi'(R_{x_j, y_j}/Q_p)}{Q_p}\right)^2 \sigma_n^2. \quad (11)$$

Hence, the received pixel value is Gaussian around the ideal (noise-free) response:

$$\begin{aligned} PV_j^{\text{re}}(b_{j-1}, b_j, b_{j+1}) \\ \sim \mathcal{N}\left(PV_j^{\text{tot}}(b_{j-1}, b_j, b_{j+1}), \sigma_n'^2(b_{j-1}, b_j, b_{j+1})\right). \end{aligned} \quad (12)$$

In general, the equivalent pixel-domain noise variance depends on the neighboring-bit pattern through the nonlinear camera response. In our experiments, the received pixel values lie in a mid-range region where the variation of  $\Phi'(\mu_j)$  across dominant triplets is small. We therefore use a *locally homoscedastic approximation* with one effective variance  $\sigma_n'^2$  per working condition for analytical tractability. For stronger nonlinearity or larger signal excursions, a triplet-dependent variance model would be more appropriate.

**Lemma 1** (Monotonicity  $\Rightarrow$  worst-case neighbors). *Let the detector use a fixed threshold  $PV_{\text{th}}$  and Gaussianized noise with standard deviation  $\sigma_n'$  independent of the bits, and nonnegative adjacent contributions  $R_{x_j, y_j}^{j-1}, R_{x_j, y_j}^{j+1} \geq 0$ . Define*

$$\mu_i(b_{j-1}, b_{j+1}) \triangleq PV_j^{\text{tot}}(b_{j-1}, i, b_{j+1}), \quad i = 0, 1.$$

*Then, conditional error probabilities are monotone in each neighbor bit:*

$$P(\hat{b}_j = e \mid b_{j-1}, b_j = i, b_{j+1}) = Q\left(\frac{PV_{\text{th}} - \mu_i(b_{j-1}, b_{j+1})}{\sigma_n'}\right),$$

*where  $Q(\cdot)$  is strictly decreasing. Hence, the worst-case neighbor patterns are  $(b_{j-1}, b_{j+1}) = (1, 1)$  for  $b_j = 0$  and  $(0, 0)$  for  $b_j = 1$ .*

*Proof.* We show monotonicity in  $b_{j-1}$ ; the argument for  $b_{j+1}$  is identical.

**Case  $b_j = 0$ .** Fix  $b_{j+1}$ . When  $b_{j-1}$  flips from 0 to 1, the conditional mean  $\mu_0$  **increases** by  $R_{x_j, y_j}^{j-1} \geq 0$  while  $\sigma_n'^2$  and  $PV_{\text{th}}$  stay fixed. Because  $Q(x)$  is strictly decreasing in  $x$ ,

$$Q\left(\frac{PV_{\text{th}} - \mu_0(1, b_{j+1})}{\sigma_n'}\right) > Q\left(\frac{PV_{\text{th}} - \mu_0(0, b_{j+1})}{\sigma_n'}\right).$$

Therefore  $P(\hat{b}_j = 1 \mid b_{j-1}, b_j = 0, b_{j+1})$  **increases** with  $b_{j-1}$ . By symmetry in  $b_{j+1}$ , the error is maximized at  $(b_{j-1}, b_{j+1}) = (1, 1)$ .

**Case  $b_j = 1$ .** Fix  $b_{j+1}$ . When  $b_{j-1}$  flips from 0 to 1, the conditional mean  $\mu_1$  **increases** by  $R_{x_j, y_j}^{j-1} \geq 0$ . Using the same monotonicity of  $Q(\cdot)$ ,

$$Q\left(\frac{\mu_1(1, b_{j+1}) - PV_{\text{th}}}{\sigma_n'}\right) < Q\left(\frac{\mu_1(0, b_{j+1}) - PV_{\text{th}}}{\sigma_n'}\right).$$

Hence  $P(\hat{b}_j = 0 \mid b_{j-1}, b_j = 1, b_{j+1})$  **decreases** with  $b_{j-1}$ . By symmetry, the error is maximized at  $(b_{j-1}, b_{j+1}) = (0, 0)$ .

Combining both cases yields the stated worst-case neighbor patterns.  $\square$

**Remark (The midpoint threshold).** The ‘‘worst-neighbor’’ ordering and the resulting bounds require a fixed threshold, a location-family statistic  $X = \mu(b_{j-1}, b_j, b_{j+1}) + n$  with nonnegative neighbor shifts (flipping  $0 \rightarrow 1$  does not decrease the mean), and noise with a monotonically decreasing tail. With approximately equal variances for  $b_j \in \{0, 1\}$  and equal

priors, the Bayes threshold for the hardest pair (1, 0, 1) vs. (0, 1, 0) is the midpoint

$$PV_{th} = \frac{1}{2} PV_j^{tot}(1, 0, 1) + \frac{1}{2} PV_j^{tot}(0, 1, 0). \quad (13)$$

Otherwise, use the LLR-root threshold. We adopt a single-variance approximation, leading naturally to the midpoint threshold as a practical decision boundary. This simplification provides analytical tractability. A detailed performance-gap quantification is left for future work.

**Theorem 1** (Analytic per-segment BER under adjacent-only ISI with worst-case midpoint threshold). *Consider the per-segment decision at  $(x_j, y_j)$  under the adjacent-only ISI model with nonnegative taps and Gaussianized noise  $n \sim \mathcal{N}(0, \sigma_n'^2)$  independent of the bits. Using the fixed threshold  $PV_{th}$  in (13), the conditional decision statistic for a given triplet  $(b_{j-1}, b_j = i, b_{j+1})$  is Gaussian with mean  $PV_j^{tot}(b_{j-1}, i, b_{j+1})$  and variance  $\sigma_n'^2$ . The conditional error probability is*

$$P(\hat{b}_j \neq i | b_{j-1}, i, b_{j+1}) = Q\left(\frac{|PV_{th} - PV_j^{tot}(b_{j-1}, i, b_{j+1})|}{\sigma_n'}\right). \quad (14)$$

In our system, a light trail forms a continuous arc in physical space but is sampled on the discrete pixel grid of the image sensor. This pixel-grid sampling induces a geometric asymmetry that depends on the relative alignment between the trail center and the pixel lattice. As a result, the shape and area of the pixel region covered by a given segment can vary slightly with position, introducing a mild position-dependent bias in the pixel value at each segment centroid. To mitigate this discretization bias, we evaluate the overall BER as the average of the per-segment BERs across all  $J$  segments.

Marginalizing the conditional error in (14) over the priors of the current bit and its two neighbors, and averaging over all segments  $j$  to capture residual discretization differences, yields the following BER expression:

$$\text{BER} = \frac{1}{J} \sum_{j=0}^{J-1} \sum_{i \in \{0,1\}} \pi_i \sum_{(b_{j-1}, b_{j+1}) \in \{0,1\}^2} \pi_{nb}(b_{j-1}, b_{j+1}) Q\left(\frac{|PV_{th} - PV_j^{tot}(b_{j-1}, i, b_{j+1})|}{\sigma_n'}\right), \quad (15)$$

where  $\pi_i = P(b_j = i)$  and  $\pi_{nb}(b_{j-1}, b_{j+1}) = P(b_{j-1}, b_{j+1})$ .

**Remark. (When is adjacent-only ISI enough?)**

Adjacent-only ISI is adequate when the *leakage ratio*

$$\Lambda_2 \triangleq \sum_{|m| \geq 2} R_{x_j, y_j}^{j+m} / \sum_{|m|=1} R_{x_j, y_j}^{j+m}$$

satisfies  $\Lambda_2 \leq \varepsilon$  for a small tolerance (e.g.,  $\varepsilon = 0.1$ ). This means that the energy leaked from non-adjacent trails is small compared with that from the immediate neighbors.

In practice,  $\Lambda_2$  stays small whenever the *tangential spacing*  $S = r_i \Delta\theta$  is sufficiently larger than the effective blur scale  $\sigma_{\text{eff}}$ . A convenient rule of thumb is  $S/\sigma_{\text{eff}} \gtrsim 1.5$ , under which the energy contribution from non-adjacent segments becomes negligible compared with that from adjacent ones. This condition typically corresponds to the regime where (i) the per-bit angular spacing is not too small (e.g.,  $r_i \Delta\theta \gtrsim \frac{1}{2} r_{\text{LED}}$ ,

TABLE I  
SIMULATION PARAMETERS.

Transmitter	
Radius of LED chip ( $r_{\text{LED}}$ )	$2.0 \times 10^{-3}$ m
Rotation radius ( $r_i$ /m)	$17.5 \times 10^{-3}$ - $94.5 \times 10^{-3}$
Control angle per bit ( $\Delta\theta$ )	$\frac{\pi}{29}$ - $\frac{\pi}{4}$ rad
Total LED transmission power ( $P_{\text{tot}}$ )	0.2 W
Channel	
Transmission distance ( $D$ )	46.0 - 62.0 m
Optical path loss coefficient ( $\gamma$ )	2.0
Transmittance of the optical filter ( $T_s$ )	0.9
FOV ( $\epsilon_l$ ), Lens gain ( $g$ )	$15^\circ$ , 1.0
Order of the Lambertian emission ( $m'$ )	1.0
S.D. of Gaussian filter ( $\sigma_g$ )	1.0-1.5
Filter Size ( $q$ )	5
S.D. of camera noise ( $\sigma_n'$ )	4.065
Receiver	
Image sensor resolution	$4000 \times 3000$ pixels
Image sensor pixel pitch ( $\rho$ )	$1.85 \times 10^{-6}$ m
Camera focal length ( $f$ )	$30 \times 10^{-3}$ m
Quantum efficiency ( $Q_e$ )	0.5
Reference voltage ( $V_{\text{ref}}$ )	3.1 V
Sense node gain ( $A_n$ )	$2.8 \times 10^{-4}$ V/e
Source follower gain ( $A_f$ )	1.0
Maximum ADC voltage ( $V_{a,\text{ref}}$ )	2.5 V
ADC gain ( $A_a$ ), CDS gain ( $A_c$ )	1.0, 1.0
Maximum RAW value ( $raw_{\text{max}}$ )	4095
Gamma value ( $g_a$ )	2.2

and (ii) the defocus blur does not spread appreciably beyond the nearest trails. If these conditions are violated (small  $\Delta\theta$ , large distance, or heavy blur), a generalized  $K$ -neighbor model should be used.

## V. SIMULATION RESULTS

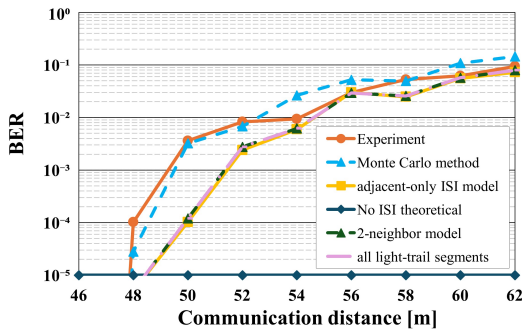
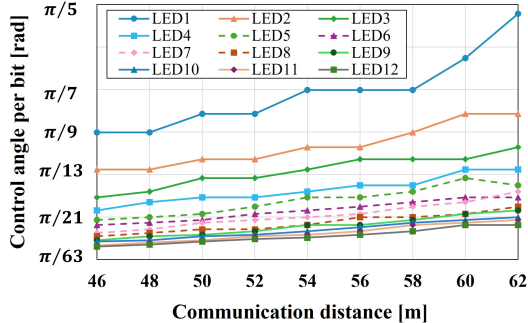
### A. Experimental Setup and Parameter Estimation

Table I lists the simulation/experimental settings. Per distance, the pixel-domain noise level is estimated from real images via *maximum-brightness extraction* [12]: we record 557 frames under a fixed blink, take the framewise maxima, apply GAT+whitening, and use their variance as  $\sigma_n'^2$ . Fig. 3 indicates near-homoscedasticity across  $b_j \in \{0, 1\}$ , so we use a single  $\sigma_n'^2$  per distance. The operating points lie in the mid-range linear region of the camera response, ensuring the validity of the local linearization and near-homoscedastic approximation. Blur parameters were fit by image-simulation matching.

### B. Simulation Results

1) *Validation of the Analytic BER Model:* Fig. 4 compares the BER against Monte Carlo simulations and experimental measurements as a function of communication distance from 46 m to 62 m at  $\Delta\theta = \pi/9$ .

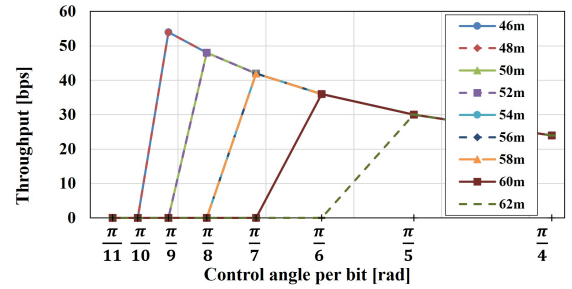
Our adjacent-only ISI model closely tracks the experimental BER and Monte Carlo BER over all tested distances. Incorporating the next-nearest neighbors (2-neighbor model) and the **all-segment** model, which considers the entire light trail, do not generally improve accuracy. In contrast, the ‘‘No ISI theoretical’’ curve assumes isolated segments with no inter-symbol interference, substantially underestimates the observed BER. Overall, the results confirm that adjacent-only ISI dominates the error behavior in this system and is sufficient for accurate BER prediction and link design. In tested conditions, the numerical results also indicate that the BER difference between the midpoint and the optimal threshold is negligible.


 Fig. 4. BER vs. communication distance ( $\Delta\theta = \pi/9$ ).

 Fig. 5. Control angle ( $\Delta\theta$ ) versus communication distance.

2) *Optimization of control angle:* The control angle  $\Delta\theta$  governs the trade-off between the data rate and communication reliability: decreasing  $\Delta\theta$  improves the data rate but reduces the spatial resolution per bit, making the signal more susceptible to ISI. Therefore, we determine the optimal control angle  $\Delta\theta$  under an error-free criterion, defined as  $\text{BER} \leq 10^{-4}$ . In the optimization, we restrict  $J$  to positive even integers ( $J = 2a$  with  $a \in \mathbb{N}$ ), thus the vertical axis is discretized at  $\pi/a$ .

Fig. 5 shows the optimal control angle  $\Delta\theta$  versus communication distance for all LEDs. Two trends are clear: (1) For each LED, the optimal  $\Delta\theta$  grows with distance, as longer distances reduce pixels per bit, increasing ISI susceptibility. (2) At fixed distance, outer LEDs need smaller  $\Delta\theta$  since their longer trails per angle mitigate ISI. In essence, as distance increases, the blur scale grows, and thus the optimal control angle also increases. We summarize this as a scaling insight:  $\Delta\theta^* \propto \frac{\sigma_{\text{eff}}(D)}{r}$ . This gives a clear design rule, linking the observed trend to a geometry–blur tradeoff.

3) *Throughput:* We define throughput as the number of bits received per unit of time under ideal conditions. In this baseline, we assume uncoded transmission, no guard angles, no inter-LED interference, perfect synchronization, and constant rotation speed. With three rotations per unit time, the data rate is  $3 \cdot 2\pi/\Delta\theta$  [bps]. Fig. 6 shows the throughput for different  $\Delta\theta$  for the innermost LED ( $i = 1$ ) at various communication distances. The resulting  $\Delta\theta$  is locally optimal within this model. While the current setup provides only a modest throughput, the achievable rate can be significantly increased by using higher-speed motors and higher frame rate image sensors. Future work will consider coding, guard angles, synchronization errors, and multi-LED effects.


 Fig. 6. Throughput vs. control angle per bit ( $\Delta\theta$ ).

## VI. CONCLUSION

We developed an analytical model for light-trail ISC with a rotating-pattern transmitter. By focusing on adjacent-trail ISI and adopting the hardest-pair midpoint threshold, we obtained a closed-form BER that matches Monte Carlo/measurements across tested settings, indicating non-adjacent trails are negligible for performance prediction. The analysis clarifies how distance, blur, and the per-bit control angle  $\Delta\theta$  shape BER and provides a practical rule to select  $\Delta\theta$ . We demonstrated throughput maximization under an error-free target. Future work will relax the adjacent-only assumption (larger  $K$ ), cover stronger blur/longer ranges/off-axis geometry, and explore decision rules that retain interpretability and efficiency.

## REFERENCES

- [1] T. Komine and M. Nakagawa, "Fundamental analysis for visible-light communication system using LED lights," *IEEE Trans. Consum. Electron.*, vol. 50, no. 1, pp. 100–107, 2004.
- [2] H. B. C. Wook, S. Haruyama, and M. Nakagawa, "Visible light communication with LED traffic lights using 2-dimensional image sensor," *IEICE Trans. Fundam. Electron. Commun. Comput. Sci.*, vol. E89-A, no. 3, pp. 654–659, Mar. 2006.
- [3] K. Kamakura, "Image sensors meet LEDs," *IEICE Trans. Commun.*, vol. E100-B, no. 6, pp. 917–925, Jun. 2017.
- [4] T. Nagura, T. Yamazato, M. Katayama, T. Yendo, T. Fujii, and H. Okada, "Tracking an led array transmitter for visible light communications in the driving situation," in *Proc. 7th Int. Symp. Wireless Comm. Syst. (ISWCS)*, 2010, pp. 765–769.
- [5] S. Arai, H. Matsushita, Y. Ohira, T. Yendo, D. He, and T. Yamazato, "Maximum likelihood decoding based on pseudo-captured image templates for image sensor communication," *NOLTA, IEICE*, vol. 10, no. 2, pp. 173–189, Apr. 2019.
- [6] S. Motwani, "Tactical drone for point-to-point data delivery using laser-visible light communication (l-vlc)," in *Proc. 3rd Int. Conf. Adv. Commun. Technol. Netw. (CommNet)*, 2020, pp. 1–8.
- [7] H. Takano, D. Hisano, M. Nakahara, K. Suzuoki, K. Maruta, Y. Onodera, R. Yaegashi, and Y. Nakayama, "Visible light communication on led-equipped drone and object-detecting camera for post-disaster monitoring," in *Proc. IEEE 93rd Veh. Technol. Conf. (VTC2021-Spring)*, 2021, pp. 1–5.
- [8] Z. Tang, S. Arai, and T. Yamazato, "Simplified alamouti-type space-time coding for image sensor communication using rotary led transmitter," *IEEE Photon. J.*, vol. 14, no. 1, pp. 1–7, 2022.
- [9] S. Arai, Z. Tang, A. Nakayama, H. Takata, and T. Yendo, "Rotary led transmitter for improving data transmission rate of image sensor communication," *IEEE Photon. J.*, vol. 13, no. 4, pp. 1–11, 2021.
- [10] Z. Tang, J. Zheng, T. Yamazato, and S. Arai, "Image sensor communication via light trail using propeller led transmitter," *IEEE Photon. J.*, vol. 15, no. 5, pp. 1–12, 2023.
- [11] S. Asaoka, S. Lu, T. Yamazato, and Z. Tang, "Theoretical modeling and interference prevention of light trails for led-propeller based image sensor communication," *IEICE Commun. Express*, pp. 1–4, 2025.
- [12] A. Liu, W. Shi, M. Ouyang, and W. Liu, "Characterization of optical camera communication based on a comprehensive system model," *J. Lightw. Technol.*, vol. 40, no. 18, pp. 6087–6100, 2022.
- [13] S. Arai, S. Mase, T. Yamazato, T. Endo, T. Fujii, M. Tanimoto, K. Kidono, Y. Kimura, and Y. Ninomiya, "Experimental on hierarchical transmission scheme for visible light communication using LED traffic light and high-speed camera," in *Proc. IEEE 66th Veh. Technol. Conf. (VTC2007-Fall)*, 2007, pp. 2174–2178.